Journal of Materials Chemistry A

Accepted Manuscript

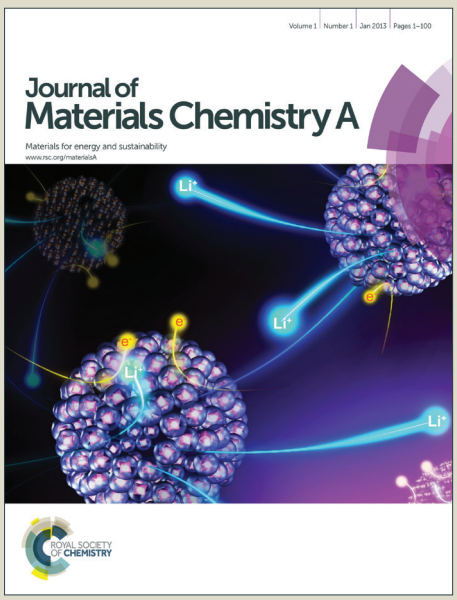

ROYAL SOCIETY OF CHEMISTRY

www.rsc.org/materialsA

Fe, Co, N-functionalized carbon nanotubes in situ grown on 3D porous N-doped carbon foams as noble metal-free catalyst for oxygen reduction

Ruizhong Zhang,[a,b] Shuijian He,[a,b] Yizhong Lu,[a,b] and Wei Chen *[a]

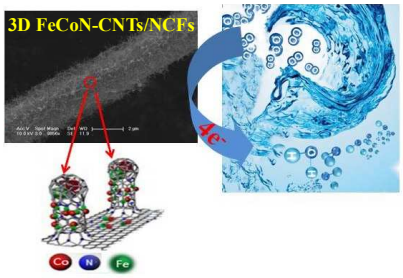

3D Fe, Co, N-functionalized carbon nanotubes grown on carbon foam were fabricated and the hybrid exhibits high ORR electrocatalytic performance.

Cite this: DOI: 10.1039/c0xx00000x

www.rsc.org/xxxxxx

ARTICLE TYPE

Fe, Co, N-Functionalized Carbon Nanotubes in situ Grown on 3D Porous N-Doped Carbon Foams as Noble Metal-Free Catalyst for Oxygen Reduction

Ruizhong Zhang,[a,b] Shuijiang He,[a,b] Yizhong Lu,[a,b] and Wei Chen[a]*

Received (in XXX, XXX) Xth XXXXXXXXX 20XX, Accepted Xth XXXXXXXXX 20XX
DOI: 10.1039/b000000x

Designing and manipulating advanced oxygen reduction reaction (ORR) electrocatalysts are of critical importance for the widespread application of fuel cells. In this work, we report a highly versatile and one-pot pyrolysis route to the mass production of a novel three-dimensional N, Fe, Co-functionalized carbon nanotubes rigidly grown on N-doped carbon foams (3D FeCoN-CNTs/NCFs) serving as noble-metal free catalyst for the oxygen reduction reaction (ORR). Different from the previously reported carbon materials, in the present 3D porous structure, the N, Fe, Co-doped carbon nanotubes are rigidly grown on the skeleton of 3D nitrogen-doped carbon foams (NCFs), showing high electrochemical stability. Moreover, due to the synergistic effect of the Fe/Co and the N species with the formation of Fe/Co-N_x complexes in the 3D hybrid carbon material, and the multiple active sites on the porous structure, the 3D hybrid displayed superior catalytic performance for ORR, high operation stability and stronger methanol/CO crossover resistance in alkaline medium. The stable porous structure and the excellent catalytic performance make the 3D FeCoN-CNTs/NCFs a promising non-precious-metal cathodic electrocatalyst for fuel cells.

1. Introduction

The increasing demand for clean energy and energy-efficient devices is becoming more and more critical owing to the depletion of conventional energy sources and serious environmental problems caused by large-scale use of fossil fuels. This urgent situation has triggered extensive research on fuel cells that have been considering promising energy-converting devices because of their high efficiency and environmental benignity.[1-3] The oxygen reduction reaction (ORR)—one of the two half-reaction in fuel cells, is one of the bottlenecks that has prevented fuel cells from finding a wide range of applications today. This is due to the inherently sluggish ORR process and the requirements of inexpensive and sustainable ORR electrocatalysts with not only efficient catalytic performance but also earth-abundant elements. Among the used ORR catalysts, platinum (Pt) and its alloys have remained the most efficient ORR catalytic performance. However, due to the limited availability, high-cost and easy corrosion, Pt-based electrocatalysts remain one of the major obstacles for large-scale commercialization of fuel cells.

In searching for more robust and practical catalysts with lower price and comparative or even better catalytic performance than Pt, much attention has been devoted to rational design of non-precious-metal or metal-free catalysts with unique architectures to dramatically enhance ORR activity. Among them, a broad range of alternative catalysts based on non-precious metals (Fe, Co, etc.)[1, 4-7] or metal oxides (Fe_2O_3, Fe_3O_4, Co_3O_4,etc.)[8-13] as well as nitrogen-coordinated metal on carbon[14-16] and metal-free doped carbon materials[17, 18] have been actively pursued. Metal or metal oxide catalysts frequently suffer from dissolution, sintering, and agglomerations during operation of fuel cells, which can result in sever catalyst degradation.[19] To overcome this obstacle, nanostructured catalyst supports such as carbon materials (active carbon, carbon nanotubes, graphene, and porous carbon etc.), metal, carbide, mesoporous silica, and conducting polymers have been developed to maximize the electroactive surface area of catalysts and improve their catalytic activity and durability.[19] Of them, porous carbon materials exhibit outstanding advantages, such as high surface area, thermal and chemical stability, good electrical conductivity, and hydrophobic surface properties, which render them suitable for potential applications as energy storage materials, and catalyst supports[20-22]. However, carbon materials themselves show low catalytic activity towards the ORR because their surfaces are chemically inert.[23] The incorporation of heteroatoms into carbon frameworks, such as mesoporous carbons, carbon nanotubes, [24, 25] graphene [26, 27] through post hoc and/or in situ doping, can not only alter the properties ranging from electrical conductivity, oxidation stability to the surface chemical states, but also improve their catalytic properties and durability for ORR. Quantum mechanics calculations[24] revealed that the enhanced catalytic activity of nitrogen-doped carbon materials could be ascribed to the net positive charge on the adjacent carbon atoms induced by the doped nitrogen atoms. The activated carbon can function as electrocatalytic active sites to facilitate the adsorption of oxygen molecule, to promote O-O bond cleavage, and further to

accelerate ORR kinetic process. Nevertheless, the common approaches for the fabrication of active carbon nanomaterials involve chemical vapor deposition (CVD), thermal annealing with nitrogen-containing chemicals, and nitrogen plasma treatment, which usually suffer from complicated manipulation, high production cost and corrosive precursors. Later, the carbonaceous materials enriched with very high nitrogen content can be readily obtained through the pyrolysis of the nitrogen-rich materials, which can serve as potential metal-free catalysts for ORR. Despite tremendous achievements, there is still considerable room for improving catalytic performance and preparation of carbonaceous materials.

Over the past years, intense investigations have also been devoted to exploring low-cost and efficient ORR electrocatalysts based on non-precious metals. Ever since the pioneering work of Jasinski,[28] a new class of non-precious metal electrocatalysts composed of metal/nitrogen/carbon (M/N/C, M=Fe or Co) have attracted much attention as ORR catalysts. Even though an in-depth understanding on the nature of the active sites in these catalysts that are responsible for the ORR is currently lacking, it has been identified that a majority of such potential compounds either possess doped nitrogen or metal-coordinated nitrogen species in the carbon matrix. Several reports,[14, 29-31] including one from our previous study[15] have found that Fe or/and Co plays a crucial role in creating the electrocatalytically active sites for ORR. Most of the research concentrated on the ORR catalysts obtained by pyrolyzing transition metal-containing macrocycles.[32, 33] Due to the high cost, macrocycles were recently replaced by various combinations of nitrogen-containing compounds, transition-metal inorganic salts, and carbons etc. and the resulting catalysts exhibited considerable improvements in ORR activity.

Herein, we develop a novel type of 3D Fe, Co, N-functionalized carbon nanotubes in situ grown on 3D N-doped carbon foams (3D FeCoN-CNTs/NCFs) as ORR catalyst. In the synthesis, the presence of Co and Fe can not only introduce efficient ORR active sites but also catalyze the growth of carbon nanotubes on the surface of 3D notrogen-doped carbon foam (3D NCFs). Such 3D porous hybrids can maximize the surface area of the nanostructures and fully utilize the various kinds of electrocatalytically active sites. Due to the multiple active sites of the iron/cobalt-coordinated nitrogen and nitrogen-doped carbon species existing in both the nitrogen-doped carbon foam skeletons and the array of Fe, Co, N-functionalized nanotubes, the obtained 3D FeCoN-CNTs/NCFs exhibited superior ORR activity, outstanding ability to immune methanol/CO crossover, and long-term operation durability in alkaline solution. This simple and economic method offers an alternative route to fabricate precious-metal-free electrocatalysts for practical application in fuel cells.

2. Experimental Section

2.1 Reagents and Materials

Iron (II) sulfate heptahydrate ($FeSO_4·7H_2O$, A.R. grade, ≥99.0%), Cobalt (II) chloride hexahydrate ($CoCl_2·6H_2O$, A.R. grade, 99.0~101.0 %), absolute ethanol (CH_3CH_2OH, A.R. grade, ≥99.7%) and methanol (CH_3OH, A.R. grade, ≥99.5%) were obtained from Beijing Chemical Works. 20%E-TEK Pt/C was purchased from Alfar Aesar. Melamine foam was supplied by Puyang Green Universh Chemical Co., Ltd. All chemicals were used as received without further purification. Ultrapure N_2 and O_2 (supplied by the Changchun Juyang gas Limited Liability Company) were used for de-aeration and the oxygen reduction reaction tests, respectively. And all aqueous solutions were prepared with ultrapure water supplied by a Water Purifier Nanopure water system (18.3 MΩ cm).

2.2 Materials Preparation

In a typical synthesis, several slices (0.2486 g) of commercially available melamine foam was soaked in the pre-prepared 80 mL 0.002 M $FeSO_4$ and $CoCl_2$ mixed aqueous solution in a vessel. The vessel was then placed in a water bath under stirring for several hours at room temperature to make the sufficient adsorption of Fe^{2+} and Co^{2+} on the melamine foam. This melamine foam impregnated with Fe^{2+} and Co^{2+} was thoroughly dried at 70 ^oC for 12 h and then pyrolyzed under Ar atmosphere at 800 ^oC for 1 h (with a heating rate of 3 ^oC/min). The carbonized catalyst was leached with 2 M H_2SO_4 at 60 ^oC for 3 h to remove unstable species and excess metals and metallic oxides. The resulting product (denoted as 3D FeCoN-CNTs/NCFs) was separated by centrifugation, washed with ultrapure water and absolute alcohol for several times, and finally dried in a drying oven. For comparison, the nitrogen-doped carbon foams decorated with single metal (Fe or Co) were also prepared with the same procedure in the presence of only cobalt or iron salt, which are denoted as 3D Fe/NCFs and 3D Co/NCFs, respectively. Blank carbonized nitrogen-doped carbon foams (3D NCFs) was also prepared by the same method with the absence of both Fe and Co.

2.3 Materials Characterization

The morphologies of the as-prepared materials were characterized with a XL30 ESEMFEG scanning electron microscope (FE-SEM) operating at an accelerating voltage of 20 kV, and elemental analyses of the materials were carried out using techniques of energy dispersive X-ray spectroscopy (EDXS), equipped in the FE-SEM. High-resolution TEM (HRTEM) images and the corresponding high-angle annular dark-field scanning transmission electron microscopy (HAADF-STEM) images and element analysis mapping were all carried out on a JEM-2010(HR) microscope operated at 200 kV. Powder X-ray diffraction (XRD) was performed on a D8 ADVANCE (Germany) using Cu Kα radiation with a Ni filter (λ=0.154059 nm at 30 kV and 15 mA) to examine the crystallinity of the products. X-ray photoelectron spectroscopy (XPS) measurements were performed by using a VG Thermo ESCALAB 250 spectrometer (VG Scientific) operated at 120 W. The binding energy was calibrated against the carbon 1s line.

2.4 Electrochemical measurements

Prior to deposition of the catalyst samples onto an electrode surface for electrochemical measurements, a glassy carbon (GC) electrode (3.0 mm in diameter) was first polished with alumina slurries (Al_2O_3, 0.05 μm) on a polishing cloth to obtain a mirror finish, followed by sonication in 0.1 M HNO_3, 0.1 M H_2SO_4, and

pure water for 10 min, successively. The catalyst ink was prepared by ultrasonically blending for 30 min 2 mg of the catalyst in 2 mL solution containing Nanopure water, isopropanol and 5 wt% Nafion suspension in alcohol (Solution Technology, Inc.), with ratio of 4:1:0.05 by volume. Before cyclic voltammograms (CVs) experiments, 5 μL of the ink was drop-coated on the polished GC surface using a microliter syringe followed by drying at room temperature, resulting in a catalyst loading of 5 μg.

Voltammetric and chronoamperometric i-t measurements were carried out with a CHI660D electrochemical workstation in a conventional three-electrode system. The working electrode was the GC covered with the catalyst samples. A platinum coil and Ag/AgCl (saturated KCl, aq.) electrodes were used as counter and reference electrodes, respectively. All electrode potentials in the present study were referred to this Ag/AgCl reference. The electrolyte was deaerated by purging high-purity N_2 gas into the electrolyte for at least 30 min before each electrochemical measurement and the catalyst samples on the GC electrodes were first electrochemically cleaned by sweeping the potential in the range between -0.95 and 0.2 V (vs. Ag/AgCl) at 100 mV/s in a N_2-saturated 0.1 M KOH solution until steady state CVs were obtained.

The electrocatalytic activities of the catalyst samples for ORR were also studied with the rotating disk electrode (RDE) and rotating ring disk electrode (RRDE) techniques using a Pine electrochemical system (from Pine Instruments Co. Ltd. USA). Before RDE and RRDE measurements, 20 μl 1 mg/mL of the catalyst ink was dropped on the clean GC disk electrodes (5 mm in diameter for RDE and 5.61 mm in diameter with a Pt ring for RRDE). All the measurements were carried out on a CHI750D electrochemical workstation assembled with a model of a Pine's Modulated Speed Rotator servo-system. Linear sweep voltammetry (LSV) measurements for ORR were performed in O_2-saturated 0.1 M KOH by cathodically sweeping the potential from 0.2 to -0.95 V at a scan rate of 10 mV/s with the electrode rotation rates of 225, 400, 625, 900, 1225, 1600 rpm. In the RRDE measurements, the Pt ring potential was set at 0.5 V (vs. Ag/AgCl). All electrochemical experiments were carried out at room temperature.

3. Results and Discussion

3.1 Synthesis and characterization of 3D N, Fe, Co-functionalized carbon nanotubes rigidly grown on N-doped carbon foam (3D FeCoN-CNTs/NCFs) nanostructure.

In the present study, a simple impregnation and one-step pyrolysis strategy was developed to synthesize the 3D FeCoN-CNTs/NCFs nanostructure using inexpensive iron and cobalt salts, and industrially available melamine foam as precursors. Melamine foam, which represents a favorable combination of aromatic rings connected via nitrogen-containing groups, is a promising template compound for nitrogen and carbon materials. Because of the structural similarity of melamine foam and graphite, the heating treatment of melamine foam could facilitate the incorporation of nitrogen-containing active sites into the graphitized 3D carbon matrix. Furthermore, the use of such a polymer as a nitrogen precursor can realize the uniform distribution of nitrogen sites on the surface and increase the active-site density. Meanwhile, during the high-temperature carbonization process, the iron and cobalt salts can be converted to non-precious metal Fe/Co-coordinated nitrogen electrocatalytically active centers. Interestingly, the formed alloy FeCo nanoparticles serve as catalytic centers for in situ growth of N-doped carbon nanotubes on the 3D carbon foam. Therefore, in the present study, through a one-pot pyrolytic process we prepared 3D hybrid nanostructure, which represents a novel non-precious metal electrocatalyst with large surface area and multiple catalytically active sites. For comparison, 3D nitrogen-doped carbon foams (3D NCFs) and NCFs doped with single Fe or Co (denoted as 3D Fe/NCFs and 3D Co/NCFs, respectively) were also synthesized.

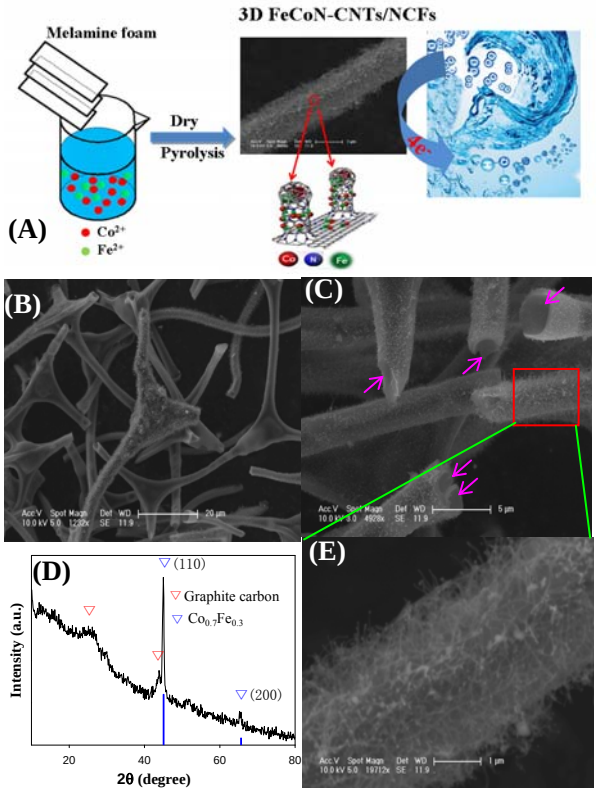

Fig. 1 (A) Schematic illustration of the preparation of the 3D FeCoN-CNTs/NCFs as ORR catalyst. (B, C and E) SEM images of the 3D hybrid nanostructure at different magnifications. The pink arrows in C show the tubulate structure of the NCFs framework. (D) XRD pattern of the 3D FeCoN-CNTs/NCFs.

As shown in Fig. 1A, the 3D FeCoN-CNTs/NCFs were synthesized via one-step pyrolysis of low-cost and commercially available melamine foam in the presence of Fe and Co salts. The morphologies of the carbonized melamine foam (3D NCFs) and transition metal-incorporated 3D nanostructures were first characterized by SEM. Fig. S1 show the representative SEM images of the 3D NCFs, which composed of branched fibers with a diameter of several micrometers and these branches entwine each other to form 3D typical open-cell network structure. After pyrolysis of the porous melamine foam loaded with iron and cobalt salts at 800 °C under Ar atmosphere for 1h, the obtained product still maintained the intrinsically 3D frame of melamine foam (Fig. 1B). From the magnified SEM image shown in Fig.

S1C, the 3D NCFs has a very smooth surface. However, for the 3D FeCoN-CNTs/NCFs, it can be seen from Fig. 1C, E that the skeleton of the nitrogen-doped carbon foam is fully covered by a layer of densely packed carbon nanotubes. It is interesting that in addition to the carbon nanotubes vertically grown on the surface of the carbon foam, the 3D carbon network actually has hollow structure, as indicated by the pink arrows in Fig. 1C. These SEM characterizations clearly show that 3D nanotube-on-microtube structure has been fabricated through the simple pyrolysis process. On the other hand, Fe-Co alloy nanocrystals have also been formed inside/outside of the N-CNTs. The corresponding energy dispersive X-ray (EDX) spectroscopy (not shown here) indicates that there are nearly equal iron (2.97 at.%) and cobalt (2.74 at.%) content in the 3D nanostructure except for the carbon (82.46 at.%) and nitrogen (4.29 at.%). The high nitrogen content may improve the electrocatalytic activity of the 3D hybrids for ORR. By analyzing randomly selected one hundred and fifty carbon nanotubes and iron cobalt hybrid nanoparticles, the average outer diameter of the carbon nanotubes is 38.06 ± 0.8 nm and the average size of the iron cobalt alloy nanoparticles is about 51.6 ± 0.3 nm (Fig. S2A and B). We also studied the 3D nanostructure carbonized from melamine foam impregnated with single metal precursor (3D Fe/NCFs and 3D Co/NCFs). The SEM images of the as-prepared 3D Fe/NCFs (Fig. S3A, B) and 3D Co/NCFs (Fig. S3C, D) show that no carbon nanotubes were formed on the surface of carbon foam, and the Fe or Co nanoparticles seriously aggregated and they are nonuniformly distributed on the nitrogen-doped carbon foam skeleton. These results indicate that the single metal precursor may be not favorable for the growth of carbon nanotubes under the present condition. Therefore, compared to the 3D Fe/NCFs and 3D Co/NCFs, the 3D FeCoN-CNTs/NCFs hybrid should have larger surface area and more exposed active sites due to the well dispersed FeCo nanoparticles and the robust carbon nanotubes grown on porous crbon foam, which are beneficial for its application as electrocatalyst.

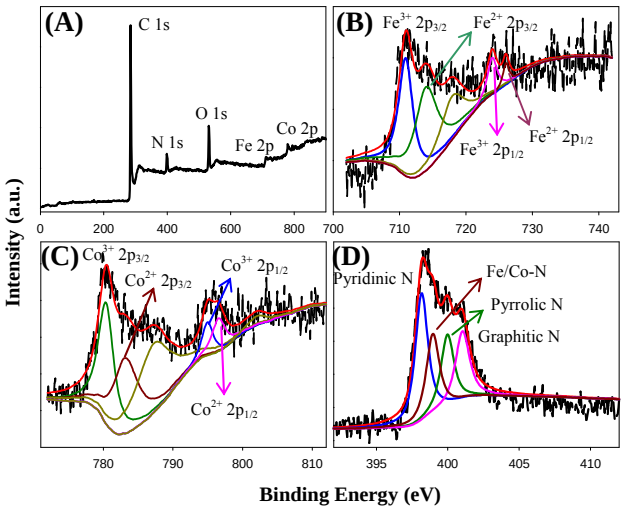

Fig. 2 XPS spectra of the 3D FeCoN-CNTs/NCFs hybrid nanostructure. (A) Survey spectrum, and high-resolution XPS spectra of Fe_{2p} (B), Co_{2p} (C) and N_{1s} (D).

From the XRD pattern of the as-prepared 3D FeCoN-CNTs/NCFs nanostructure shown in Fig. 1D, two pronounced graphitic peaks of (002) at 26° and (101) at 43° can be observed clearly, indicating the formation of graphitic structure during the carbonization of melamine foam [34, 35]. Moreover, compared to the XRD pattern of the 3D NCFs (Fig. S4), the obvious diffraction peaks at 45.05° and 65.6° could be indexed to the (110) and (200) crystal planes of $Co_{0.7}Fe_{0.3}$ alloy (PDF # 48-1818), which strongly indicates the formation of alloyed $Co_{0.7}Fe_{0.3}$ in the 3D FeCoN-CNTs/NCFs hybrid nanostructure. It should be noted that there is no diffraction signal from any other impurities, such as single metal and metal oxides, indicating the single $Co_{0.7}Fe_{0.3}$ phase in the product. Compared with single metal phase, the alloy metal may exhibit synergetic effect for the ORR electrocatalysis.

The chemical states of C, N, Fe, Co and the composition of the 3D FeCoN-CNTs/NCFs nanostructure were further investigated by XPS measurements. Fig. 2A shows the survey spectrum of the 3D nanostructure. The five predominant peaks at 286.6, 400.2, 531.2, 709.5 and 780.2 eV correspond to the binding energies of C_{1s}, N_{1s}, O_{1s}, Fe_{2p} and Co_{2p}, respectively. This result indicates that after pyrolyzing the melamine foam soaked with the metal salts, nitrogen and metal contents have been successfully introduced into the 3D FeCoN-CNTs/NCFs nanostructure. The Fe_{2p} spectrum shown in Fig. 2B can be deconvoluted into five peaks at 710.94, 713.97, 723.96, 726.03 and 717.94, eV, corresponding to the $2p_{3/2}$ of Fe (III) and Fe (II) ions, $2p_{1/2}$ of Fe (III) and Fe (II) ions, and satellite peak respectively.[36, 37] Similarly, from the Co_{2p} spectrum shown in Fig. 2C, the deconvoluted peaks can be assigned to $2p_{3/2}$, $2p_{1/2}$ of Co (III) and Co (II) ions and shakeup satellite peaks.[38, 39] In the high-resolution N_{1s} spectrum, the four deconvoluted peaks at around 398.17, 398.95, 399.98 and 401.03 eV can be attributed to pyridinic N (24.5%), metal-bonded N (26%), pyrrolic N (23.7%) and graphitic N (25.8%), respectively.[34, 36, 40] Particularly, the presence of the iron/cobalt-coordinated nitrogen and nitrogen-doped carbon species are believed to be an important contributing factor to the enhanced ORR catalytic activity of carbon-based catalysts. The high-resolution C_{1s} spectrum (Fig. S5) can be deconvoluted into three peaks at 284.55, 285.43 and 287.07 eV, which are assigned to the C=C/C-C (51.3%), C-N (29.7%) and C-O (19.0%), respectively.[41, 42] The above SEM and XPS results indicate the co-existing of nitrogen-doped carbon and the metal (Fe and Co)-coordinated nitrogen species in the 3D porous nanostructures which provide the active and stable sites for the ORR. For comparison, the XPS spectra of the 3D NCFs nanostructure are shown in Fig. S6.

The morphology, crystal structure and elemental distribution of the 3D FeCoN-CNTs/NCFs hybrid nanostructure were further analyzed by HRTEM. Fig. 3A-C shows the HRTEM images of the 3D nanostructure at different magnifications. It can be seen clearly that the formed carbon nanotubes (CNTs) are vertically and firmly anchored on the surface of the nitrogen-doped carbon foam skeleton (Fig. 3A). On the other hand, metal nanoparticles distribute at the tip and outside of the CNTs. The magnified image shown in Fig. 3B reveals the tubulate structure of the 1D carbon materials. From the HRTEM image in Fig. 3C, well-resolved lattice fringes are present with an interplanar spacing of 0.34 nm, which can be referred to the (002) plane of graphite carbon. For further insight into the element distribution of the 3D nanostructure, scanning transmission electron microscopy (STEM)

was performed. From the elemental maps of N and C (Fig. 3G, H), one can see that the doped nitrogen evenly distribute throughout the 3D hybrid structure. Fig. 3E and F show the elemental maps of Fe and Co, respectively, from which Fe and Co mainly distribute on the carbon nanotubes. It can be proposed that with the growth of CNTs under the catalysis of Fe and Co, Fe and Co were doped in the CNTs simultaneously by forming the Fe-N_x and/or Co-N_x bonding. It can also be seen that FeCo bimetallic particles have been produced during the pyrolysis process. For instance, for the nanoparticle indicated by the red arrow in the high-angle annular dark-field (HAADF) image (Fig. 3D), it is clearly composed of both Fe and Co (Fig. 3E, F).

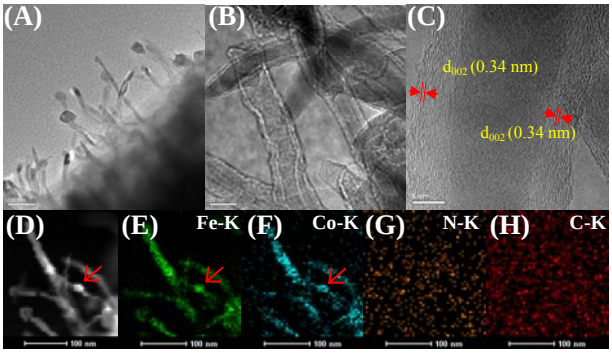

Fig. 3 (A-C) HRTEM micrographs of the 3D FeCoN-CNTs/NCFs hybrid nanostructure at different magnifications. (D) The high-angle annular dark-field (HAADF)-STEM image of 3D FeCoN-CNTs/NCFs and the corresponding element mapping of (E) Fe, (F) Co, (G) N and (H) C.

All the structure characterizations suggest that under the addition of transition metals (Fe, Co), the disordered carbon phase of carbon-nitrogen complex precursor can be transformed into graphitized structure carbon at a relatively low temperature (800 ^{o}C) owing to the catalytic function of transition metals which accelerate the graphitization process. Moreover, the transition metal species can catalyze the *in situ* growth of N-doped CNTs on the 3D carbon foam. Meanwhile, Fe and Co species can interact with amorphous carbon and thus lead to the surface rearrangement by coordinating with nitrogen and carbon within the micropores.[43, 44] It has been found that carbon nanotube-based composites exhibited extensive applications (Li-ion batteries, fuel cells and supercapacitors, etc.). However, carbon nanotube dispersion usually tends to self-agglomerate. To obtained high quality nanotubes dispersion, surface functionalization through a chemical treatment is therefore often needed, which leads to additional processing steps and high cost. The present study demonstrates that through a single pyrolysis step, 3D FeCoN-CNTs/NCFs hybrids with rigid structure and multiple catalytic centers can be easily fabricated. At the same time, it has been reported that cyanamide can be used as a carbon source for CNT synthesis.[44] This work indicates that melamine foam can serve as a promising carbon and nitrogen-containing precursor for the preparation of N-doped CNTs.

3.2. Improved electrocatalytic performance of the 3D FeCoN-CNTs/NCFs hybrid nanostructure for ORR.

To assess the ORR electrocatalytic activity of the as-prepared 3D FeCoN-CNTs/N-CMTs nanostructure, cyclic voltammetry (CV) measurements were performed in 0.1 M KOH solution at a scanning rate of 10 mV/s. As shown in Fig. 4A, a substantial cathodic ORR peak can be observed at -0.14 V with an onset potential of -0.01 V in O_2-saturated 0.1 M KOH solution. In sharp contrast, only featureless voltammetric curve was obtained in N_2-saturated electrolyte, suggesting a pronounced electrocatalytic activity of the 3D FeCoN-CNTs/NCFs nanostructure towards ORR. To gain additional insight into the effects of iron and cobalt doping on the ORR performances, the CV curves of the metal-free nitrogen-doped carbon foam (3D NCFs), 3D Fe/NCFs and 3D Co/NCFs nanostructures were also measured and shown in Fig. S7. By comparing the CVs, the 3D FeCoN-CNTs/NCFs nanostructure displays the most positive peak potential (-0.14 V) for ORR than those obtained from the 3D Fe/NCFs (-0.24 V), 3D Co/NCFs (-0.17 V) and 3D NCFs (-0.35 V). Moreover, the 3D FeCoN-CNTs/NCFs nanostructure shows an onset potential at -0.01 V, which is more positive than that from the 3D Fe/NCFs (-0.05 V), 3D Co/NCFs (-0.03 V) and 3D NCFs (-0.15 V). Remarkably, the 3D FeCoN-CNTs/NCFs nanostructure exhibits the most enhanced ORR activity with much more positive onset and peak potentials, as well as a higher cathodic current than the single metal phase composite and the pure N-doped carbon foam. Note that the present activity is also higher than the previously reported results.[36, 37, 45]

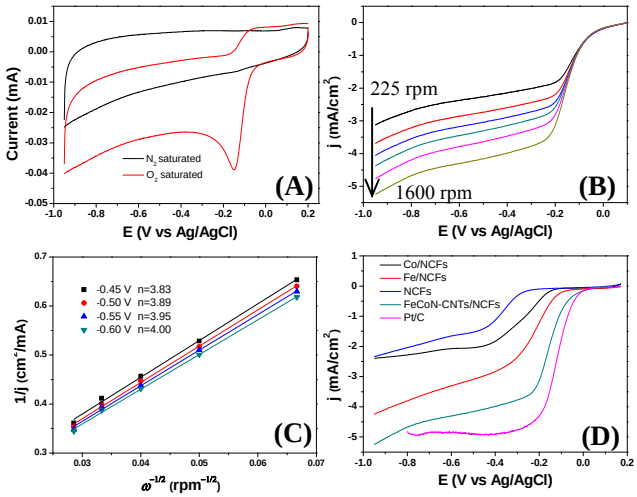

Fig. 4 (A) Cyclic voltammograms of the 3D FeCoN-CNTs/NCFs hybrid nanostructure electrode in N_2- and O_2-saturated 0.1 M KOH at a potential scan rate of 10 mV/s. (B) Rotating disk electrode (RDE) voltammograms obtained from the 3D FeCoN-CNTs/NCFs at various rotation rates. (C) Koutecky-Levich plots for ORR on the 3D FeCoN-CNTs/NCFs at different potentials. The transferred electron number per oxygen molecule in the ORR is calculated and listed in the legend. (D) Comparison of the RDE voltammograms from the studied catalysts for oxygen reduction in O_2-saturated 0.1 M KOH. Rotation rate is 1600 rpm.

To elucidate the nature of catalytic sites in the as-prepared FeCoN-CNTs/NCFs, we compared the XPS spectra of NCFs and FeCoN-CNTs/NCFs. In the N_{1s} XPS spectrum of NCFs (Fig. S6C), there are mainly pyridinic N (22.3%) and graphitic N (35%). However, in addition to the pyridinic N and graphitic N, there are two more peaks of pyrrolic N (23.7%) and Fe/Co-N (26%) in the N1s XPS spectrum of FeCoN-CNTs/NCFs (Fig. 2D).

Meanwhile, the electrochemical measurements showed that the NCFs have low catalytic activity for ORR, suggesting the low catalytic activity of pyridinic N and graphitic N for ORR. Based on the above results, although the exact nature of the active sites in the metal-nitrogen-carbon catalysts remains unknown, it seems that the pyrrolic N and Fe/Co-N_x are highly active species to enhance the ORR performance of the 3D FeCoN-CNTs/NCFs nanostructure.[46-48]

Rotating-disk electrode (RDE) measurements were also performed to further reveal the kinetics of the ORR on the 3D precious metal-free catalyst. The polarization curves of ORR on the 3D FeCoN-CNTs/NCFs hybrid nanostructure recorded from 400 to 1600 rpm in an O_2-saturated 0.1 M KOH are shown in Fig. 4B. The voltammetric profiles display that the current density can be enhanced by an increase in the rotation rate, which could be attributed to the shortened diffusion distance at high speeds. The onset potential of the 3D FeCoN-CNTs/NCFs hybrid nanostructure for ORR is at approximately -0.016 V, close to that identified from the CV measurements (-0.01 V, Fig. 4A). The corresponding Koutecky-Levich plots (J^{-1} vs $\omega^{-1/2}$) at various electrode potentials are shown in Fig. 4C, from which the good linearity and near parallelism of the fitting lines suggest the first-order reaction kinetics with respect to the concentration of dissolved O_2 and the consistent electron transfer numbers at different potentials for ORR. The kinetics parameters can be analyzed on the basis of the Koutecky-Levich equations as follows:

$$\frac{1}{j} = \frac{1}{j_k} + \frac{1}{B\omega^{1/2}} \quad (1)$$

$$B = 0.2nF\,(D_0)^{2/3}\,\nu^{-1/6}C_0 \quad (2)$$

Where j is the measured current density, j_k is the kinetic current density, ω is the electrode rotating rate, n represents the number of electrons transferred per oxygen molecule, F is the Faraday constant (F=96 485 C/mol), D_0 is the diffusion coefficient of O_2 in 0.1 M KOH (1.9×10^{-5} cm^2/s), ν is the kinetic viscosity (0.01 cm^2/s), and C_0 is the bulk concentration of O_2 (1.2×10^{-6} mol/cm^3). The constant 0.2 is used when the rotation speed is expressed in rpm. According to the equations 1 and 2, the number of transferred electrons (n) and kinetic current density (j_k) can be obtained from the slope and intercept of the Koutecky-Levich plots, respectively. The electron transferred number n was calculated to be 3.83, 3.89, 3.95 and 4.00 at -0.45, -0.5, -0.55 and -0.6 V, respectively, suggesting that the 3D FeCoN-CNTs/NCFs hybrid catalyst favors a four-electron oxygen reduction process, similar to the ORR catalyzed by a commercial Pt/C catalyst (Fig. S8). Furthermore, from the intercept of Koutecky-Levich plots, the j_k of ORR at -0.4 V from the 3D FeCoN-CNTs/NCFs hybrid was calculated to be 30.47 mA/cm^2, which is higher than that obtained from the 3D Fe/NCFs (9.01 mA/cm^2, Fig. S9B), 3D Co/NCFs (7.69 mA/cm^2, Fig. S9D) and 3D NCFs (2.18 mA/cm^2, Fig. S9F) at -0.4V. The kinetics of ORR on the 3D Fe/NCFs, 3D Co/NCFs and 3D NCFs were also investigated by RDE measurements. As seen from Fig. S9, the 3D Fe/NCFs and 3D Co/NCFs show ORR catalytic activities, but their performances are less than desirable. From the slopes of the Koutecky-Levich plots in Fig. S9B and D, the numbers of electrons transferred per O_2 molecule on the 3D Fe/NCFs and 3D Co/NCFs were calculated to be around 3.0 at different potentials. Such result suggests that the ORR on the 3D Fe/NCFs and 3D Co/NCFs electrocatalysts involve both the two-electron and four-electron processes. From Fig. S9E and F, the 3D NCFs itself exhibits very low ORR activity with an electron transfer number of about 1.55. These electrochemical results suggest that ORR on the 3D nitrogen-doped carbon foam proceeds by the inefficient two-electron pathway.

Fig. 4D summarizes the RDE voltammograms of ORR obtained from the different electrocatalysts in O_2-saturated 0.1 M KOH at 1600 rpm. It can be seen clearly that although the 3D FeCoN-CNTs/NCFs hybrid shows lower onset potential (-0.01 V) than that of the commercial Pt/C (+0.05 V), the ORR current densities from both catalysts are very close. Moreover, the 3D FeCoN-CNTs/NCFs hybrid exhibits much higher ORR catalytic performance than other studied 3D catalysts with more positive onset potential and larger limiting current density. These results indicate that the 3D FeCoN-CNTs/NCFs hybrid nanomaterial is promising precious metal-free cathodic catalyst for fuel cells with low-cost and high catalytic performance.

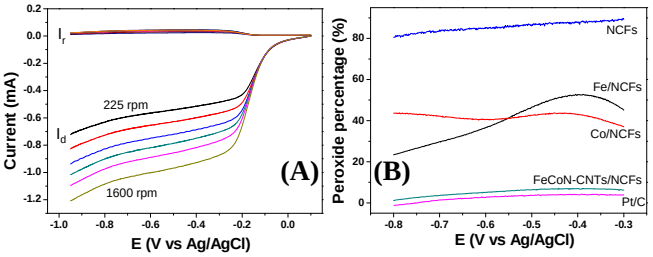

Fig. 5 (A) Rotating ring disk electrode (RRDE) measurements of oxygen reduction (I_d) and hydrogen peroxide oxidation (I_r) on the 3D FeCoN-CNTs/NCFs hybrid electrocatalyst in O_2-saturated 0.1 M KOH at different rotation rates. (B) The calculated percentages of hydrogen peroxide yield for ORR at the 3D FeCoN-CNTs/NCFs, 3D Fe/NCFs, 3D Co/NCFs, 3D NCFs and Pt/C catalysts.

By using the rotating-ring-disk electrode (RRDE) technique, the H_2O_2 yield can be accurately determined from the disk and ring currents during the ORR. The percentage of HO_2^- is determined by the following equation:

$$HO_2^-\% = \frac{200 i_R/N}{i_D + i_R/N} \quad (3)$$

Where i_D is the disk current, i_R is the ring current, and N is the current collect efficiency of the Pt ring (0.37 for this work). As shown in Fig. 5A, the disk currents from ORR are much higher than the ring currents from the H_2O_2 oxidation on the 3D FeCoN-CNTs/NCFs hybrid nanostructure at different rotation rates. Based on the disk and ring currents (equation 3), the detected H_2O_2 yield for 3D FeCoN-CNTs/NCFs hybrid is below 7% at a potential range of -0.3 to -0.8 V (vs. Ag/AgCl) and corresponding to a high electron-transfer number of above 3.88, while H_2O_2 yield for the 3D Fe/NCFs, 3D Co/NCFs and 3D NCFs are as high as 50%, 43% and 90%, respectively (Fig. 5B).

As discussed above, we studied in detail the electrocatalytic activity of the three-dimensional FeCoN-CNTs/NCFs hybrid nanostructure pyrolyzed at 800 °C. To reveal the correlation between the structure characteristics and electrochemical performance, we further studied the effects of the pyrolysis temperature (700, 800, 900 and 1000 °C) of the melamine foam

(denoted as NCFs-700, NCFs-800, NCFs-900 and NCFs-1000) on their electrocatalytic activities for ORR. In the electrochemical measurements, the NCFs-700, NCFs-800, NCFs-900 and NCFs-1000 3D catalysts were supported on a glassy-carbon RDE (catalyst loading was 0.2 mg/cm^2) and then cyclic voltammograms and linear sweep voltammograms (rotation rate of 1600 rpm) were recorded in O_2-saturated 0.1 M KOH solution. As compared in Fig. S10A, the NCFs-800 exhibits a more positive peak potential (-0.28 V) than the NCFs-700 (-0.32 V), NCFs-900 (-0.29 V) and NCFs-1000 (-0.3 V), and a larger reduction current (0.1 mA) than NCFs-700 (0.095 mA), NCFs-900 (0.074 mA) and NCFs-1000 (0.076 mA) at peak potential. Furthermore, the linear sweep voltammetric (LSV) curves in Fig. S10B show that 800 ^oC is the best carbonization temperature in terms of the ORR performance. This is because that the low-temperature carbonization cannot lead to a high graphitization degree to ensure a good conductivity, while high-temperature carbonization could lead to a decrease in the total nitrogen content. Based on such result, 800 ^oC was used as the optimal carbonization temperature for preparing all the samples in this study.

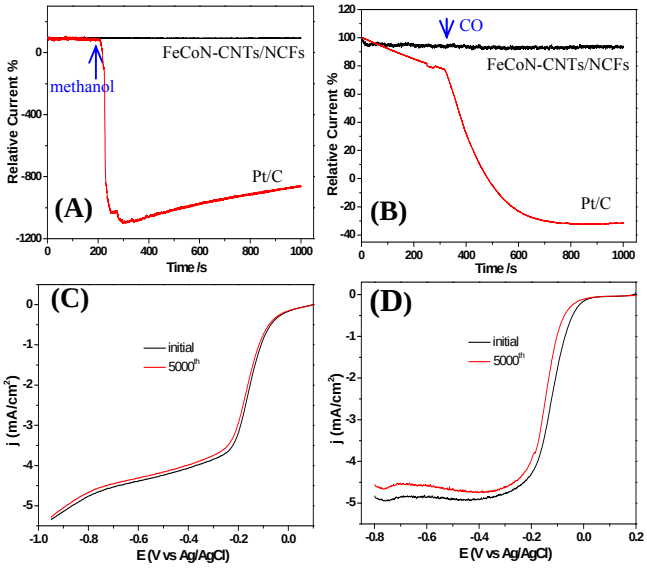

Fig. 6 Current-time chronoamperometric response of the 3D FeCoN-CNTs/NCFs hybrid and Pt/C in O_2-saturated 0.1 M KOH with a rapid addition of 1 M methanol at around 200 s (A), and gradual introduction of CO at about 300 s (B), rotation rate 1600 rpm. ORR polarization plots of the 3D FeCoN-CNTs/NCFs hybrid (C) and Pt/C (D) before and after 5000 cycles in O_2-saturated 0.1 M KOH at 1600 rpm.

Besides electrocatalytic activity, the electrochemical durability and tolerance to methanol/CO poisoning are also of extremely importance for a cathode catalyst, which is one of the major challenges faced by precious-metal-based catalysts in fuel cells. Here, chronoamperometric measurements were carried out to investigate the methanol/CO crossover effects and durability of the 3D FeCoN-CNTs/NCFs hybrid for ORR. As shown in Fig. 6A, upon addition of 1 M methanol into the electrolyte, a sharp decrease in current was observed for the Pt/C catalyst. In contrast, no obvious change was observed in the ORR current for the 3D FeCoN-CNTs/NCFs hybrid electrode, indicating its high ORR selectivity and excellent resistance to methanol crossover. As for the CO poisoning effect (Fig. 6B), the ORR current on the Pt/C electrode is gradually decreased with the gradual addition of CO to the O_2-saturated KOH, whereas the 3D FeCoN-CNTs/NCFs hybrid electrode is free from the CO poisoning. These results suggest that the 3D FeCoN-CNTs/NCFs catalyst has superior selectivity for ORR and high methanol and CO tolerance. Finally, we performed accelerated durability tests by cycling the electrocatalysts between -0.4 and 0.1 V at 0.1 V/s in O_2-saturated 0.1 M KOH to evaluate the electrochemical durability of the 3D FeCoN-CNTs/NCFs hybrid catalyst and commercial Pt/C. As shown in Fig. 6C, After 5000 continuous potential cycles, the half-wave potential exhibits a small negative shift of 9 mV and the current density (at -0.4 V) show little change of initial current dentity on the 3D FeCoN-CNTs/NCFs, while 24 mV negative shift of half-wave potential ($E_{1/2}$) and an ~ 6% loss of initial current density of ORR were observed for Pt/C (Fig. 6D). The results indicate that the 3D FeCoN-CNTs/NCFs hybrid exhibits a remarkably enhanced long-term durability compared to the commercial Pt/C catalyst.

4. Conclusion

In summary, a novel N, Fe, and Co-codoped CNTs hybrided with N-doped carbon foams catalyst (3D FeCoN-CNTs/NCFs) with a 3D porous nanostructure has been successfully fabricated. Different from the previously reported carbon materials, the present 3D carbon hybrid material provides a robust porous nanostructure and multiple catalytically active centers. The fabricated 3D structure exhibited superior catalytic performance for ORR in an alkaline medium. The unprecedented high electrocatalytic activity could be attributed to the synergistic effect of the Fe/Co and the N species with the formation of Fe/Co-N_x complexes in the carbon material. Compared with the commercial Pt/C catalyst, the optimized 3D FeCoN-CNTs/NCFs hybrid displayed higher operation stability and stronger methanol/CO crossover resistance. The stable porous structure and the excellent catalytic performance make the 3D nanostructure a promising non-precious-metal cathodic electrocatalyst for fuel cells.

Acknowledgements

This work was supported by the National Natural Science Foundation of China (No. 21275136) and the Natural Science Foundation of Jilin province, China (No. 201215090).

Notes and references

[a] *State Key Laboratory of Electroanalytical Chemistry, Changchun Institute of Applied Chemistry, Chinese Academy of Sciences, Changchun 130022, Jilin, China. Tel: +86431-85262061; E-mail: weichen@ciac.ac.cn*
[b] *University of Chinese Academy of Sciences, Beijing 100039, China*
† Electronic Supplementary Information (ESI) available: Additional structure characterizations and more electrochemical measurements of the as-prepared materials. See DOI: 10.1039/b000000x/

1. F. Jaouen, E. Proietti, M. Lefevre, R. Chenitz, J. P. Dodelet, G. Wu, H. T. Chung, C. M. Johnston and P. Zelenay, *Energy Environ. Sci.*, 2011, **4**, 114-130.
2. B. C. H. Steele and A. Heinzel, *Nature*, 2001, **414**, 345-352.

3. M. M. Liu, R. Z. Zhang and W. Chen, *Chem. Rev.*, 2014, **114**, 5117-5160.
4. A. Morozan, B. Jousselme and S. Palacin, *Energy Environ. Sci.*, 2011, **4**, 1238-1254.
5. D. S. Su and G. Q. Sun, *Angew. Chem. Int. Ed.*, 2011, **50**, 11570-11572.
6. W. T. Wei, Y. Z. Lu, W. Chen and S. W. Chen, *J. Am. Chem. Soc.*, 2011, **133**, 2060-2063.
7. H. B. Wu and W. Chen, *J. Am. Chem. Soc.*, 2011, **133**, 15236-15239.
8. W. Zhou, L. Ge, Z. G. Chen, F. L. Liang, H. Y. Xu, J. Motuzas, A. Julbe and Z. H. Zhu, *Chem. Mater.*, 2011, **23**, 4193-4198.
9. E. R. Vago and E. J. Calvo, *J. Chem. Soc., Faraday Trans.*, 1995, **91**, 2323-2329.
10. C. Medard, M. Lefevre, J. P. Dodelet, F. Jaouen and G. Lindbergh, *Electrochim. Acta*, 2006, **51**, 3202-3213.
11. Z. S. Wu, S. B. Yang, Y. Sun, K. Parvez, X. L. Feng and K. Mullen, *J. Am. Chem. Soc.*, 2012, **134**, 9082-9085.
12. Y. Y. Liang, Y. G. Li, H. L. Wang, J. G. Zhou, J. Wang, T. Regier and H. J. Dai, *Nat. Mater.*, 2011, **10**, 780-786.
13. J. J. Duan, Y. Zheng, S. Chen, Y. H. Tang, M. Jaroniec and S. Z. Qiao, *Chem. Commun.*, 2013, **49**, 7705-7707.
14. T. Palaniselvam, B. P. Biswal, R. Banerjee and S. Kurungot, *Chem. Eur. J.*, 2013, **19**, 9335-9342.
15. Y. Y. Jiang, Y. Z. Lu, X. Y. Lv, D. X. Han, Q. X. Zhang, L. Niu and W. Chen, *ACS Catal.*, 2013, **3**, 1263-1271.
16. L. Wang, J. Yin, L. Zhao, C. G. Tian, P. Yu, J. Q. Wang and H. G. Fu, *Chem. Commun.*, 2013, **49**, 3022-3024.
17. H. X. Zhong, H. M. Zhang, S. S. Liu, C. W. Deng and M. R. Wang, *ChemSusChem*, 2013, **6**, 807-812.
18. X. J. Sun, Y. W. Zhang, P. Song, J. Pan, L. Zhuang, W. L. Xu and W. Xing, *ACS Catal.*, 2013, **3**, 1726-1729.
19. Y. J. Wang, D. P. Wilkinson and J. J. Zhang, *Chem. Rev.*, 2011, **111**, 7625-7651.
20. J. Zhang, Y. S. Hu, J. P. Tessonnier, G. Weinberg, J. Maier, R. Schlogl and D. S. Su, *Adv. Mater.*, 2008, **20**, 1450-1455.
21. G. P. Hao, W. C. Li, D. Qian and A. H. Lu, *Adv. Mater.*, 2010, **22**, 853-857.
22. Y. P. Zhai, Y. Q. Dou, D. Y. Zhao, P. F. Fulvio, R. T. Mayes and S. Dai, *Adv. Mater.*, 2011, **23**, 4828-4850.
23. Y. Y. Shao, J. H. Sui, G. P. Yin and Y. Z. Gao, *Appl. Catal. B*, 2008, **79**, 89-99.
24. K. P. Gong, F. Du, Z. H. Xia, M. Durstock and L. M. Dai, *Science*, 2009, **323**, 760-764.
25. A. H. Nevidomskyy, G. Csanyi and M. C. Payne, *Phys. Rev. Lett.*, 2003, **91**, 105502.
26. H. B. Wang, T. Maiyalagan and X. Wang, *ACS Catal.*, 2012, **2**, 781-794.
27. D. S. Geng, Y. Chen, Y. G. Chen, Y. L. Li, R. Y. Li, X. L. Sun, S. Y. Ye and S. Knights, *Energy Environ. Sci.*, 2011, **4**, 760-764.
28. R. Jasinski, *Nature*, 1964, **201**, 1212-1213.
29. R. Z. Jiang and D. Chu, *J. Power Sources*, 2014, **245**, 352-361.
30. J. Wu, Z. R. Yang, X. W. Li, Q. J. Sun, C. Jin, P. Strasser and R. Z. Yang, *J. Mater. Chem. A*, 2013, **1**, 9889-9896.
31. J. Tian, A. Morozan, M. T. Sougrati, M. Lefevre, R. Chenitz, J. P. Dodelet, D. Jones and F. Jaouen, *Angew. Chem. Int. Ed.*, 2013, **52**, 6867-6870.
32. B. Wang, *J. Power Sources*, 2005, **152**, 1-15.
33. G. E. Haslam, X. Y. Chin and G. T. Burstein, *Phys. Chem. Chem. Phys.*, 2011, **13**, 12968-12974.
34. Z. H. Xiang, Y. H. Xue, D. P. Cao, L. Huang, J. F. Chen and L. M. Dai, *Angew. Chem. Int. Ed.*, 2014, **53**, 2433-2437.
35. K. Evanoff, A. Magasinski, J. B. Yang and G. Yushin, *Adv. Energy Mater.*, 2011, **1**, 495-498.
36. Y. L. Zhai, C. Z. Zhu, E. K. Wang and S. J. Dong, *Nanoscale*, 2014, **6**, 2964-2970.
37. J. Zhang, D. P. He, H. Su, X. Chen, M. Pan and S. C. Mu, *J. Mater. Chem. A*, 2014, **2**, 1242-1246.
38. R. Z. Zhang and W. Chen, *Biosens.Bioelectron.*,2014, **55**, 83-90.
39. W. T. Wang, S. Chakrabarti, Z. G. Chen, Z. F. Yan, M. O. Tade, J. Zou and Q. Li, *J. Mater. Chem. A*, 2014, **2**, 2390-2396.
40. R. Ding, L. Qi, M. J. Jia and H. Y. Wang, *Nanoscale*, 2014, **6**, 1369-1376.
41. H. L. Peng, Z. Y. Mo, S. J. Liao, H. G. Liang, L. J. Yang, F. Luo, H. Y. Song, Y. L. Zhong and B. Q. Zhang, *Sci. Rep.*, 2013, **3**, 1765.
42. A. G. Kong, B. Dong, X. F. Zhu, Y. Y. Kong, J. L. Zhang and Y. K. Shan, *Chem. Eur. J.*, 2013, **19**, 16170-16175.
43. G. Wu, M. Nelson, S. G. Ma, H. Meng, G. F. Cui and P. K. Shen, *Carbon*, 2011, **49**, 3972-3982.
44. H. T. Chung, J. H. Won and P. Zelenay, *Nat. Commun.*, 2013, **4**, 1922.
45. Y. C. Wang and X. Jiang, *ACS Appl. Mater. Interfaces*, 2013, **5**, 11597-11602.
46. Z. H. Sheng, L. Shao, J. J. Chen, W. J. Bao, F. B. Wang and X. H. Xia, *ACS Nano*, 2011, **5**, 4350-4358.
47. G. Wu, K. L. More, C. M. Johnston and P. Zelenay, *Science*, 2011, **332**, 443-447.
48. C. Z. Zhang, R. Hao, H. Yin, F. Liu and Y. L. Hou, *Nanoscale*, 2012, **4**, 7326-7329.